

MASS-CORRECTIONS FOR THE CONSERVATIVE COUPLING OF FLOW AND TRANSPORT ON COLLOCATED MESHES

CHRISTIAN WALUGA, BARBARA WOHLMUTH, AND ULRICH RÜDE

ABSTRACT. Buoyancy-driven flow models demand a careful treatment of the mass-balance equation to avoid spurious source and sink terms in the non-linear coupling between flow and transport. In the context of finite-elements, it is therefore commonly proposed to employ sufficiently rich pressure spaces, containing piecewise constant shape functions to obtain local or even strong mass-conservation. In three-dimensional computations, this usually requires nonconforming approaches, special meshes or higher order velocities, which make these schemes prohibitively expensive for some applications and complicate the implementation into legacy code. In this paper, we therefore propose a lean conservatively coupled scheme based on standard stabilized linear equal-order finite elements for the Stokes part and vertex-centered finite volumes for the energy equation. We show that in a weak mass-balance it is possible to recover exact conservation properties by a local flux-correction which can be computed efficiently on the control volume boundaries of the transport mesh. We discuss implementation aspects and demonstrate the effectiveness of the flux-corrections by different two- and three-dimensional examples which are motivated by geophysical applications.

1. INTRODUCTION

In the last decade, the importance of using locally conservative methods for coupled flow and transport problems was emphasized by many researchers in the field of computational fluid dynamics; cf., e.g., the discussions in [19, 24]. Especially in situations where we consider a long-term nonlinear and bidirectional coupling between incompressible flow and transport, the use of compatible (i.e., locally conservative) algorithms is strongly recommended, to avoid a severe violation of physical conservation principles due to the amplification of spurious sources and sinks in the flow field [19]. Such compatible algorithms often treat the subproblems separately, by ensuring that the discrete schemes yield local or even strongly conservative velocities, which are used to compute convective fluxes in a locally conservative transport scheme. Suitable schemes of arbitrary order for the transport equation are readily available [17, 34]. However, the question of conservation for the flow part is a delicate one: While it is straightforward to show local or even strong conservation properties for mixed finite element schemes with piecewise discontinuous pressure spaces, it is difficult to find schemes which are at the same time LBB stable [12]. Hence, it is a long-standing belief that local conservation properties require either penalization techniques or are limited to non-conforming, stabilized or higher order mixed finite element schemes involving velocity spaces which are rich enough to retain stability when paired with piecewise discontinuous pressures [41, 24].

AMS subject classifications: 65F10, 65N12, 65N30, 76D07, 76R10; Keywords: finite element method; finite volume method; flow/transport coupling; local mass-conservation; incompressible flow; unstructured meshes
Corresponding author: Christian Waluga (waluga@ma.tum.de), Institute for Numerical Mathematics (M2), Technische Universität München, Boltzmannstraße 3, D-85748 Garching b. München, Germany

In this work, we follow a different strategy which does not rely on flow discretizations that directly yield locally conservative velocities. We rather built upon lean stabilized discretizations for which a mature machinery of fast solvers exists, and we employ the framework established in [30] to recover conservative fluxes for the transport. Hence, in contrast to most related work, we do not treat the coupled problem as two distinct subproblems which have to satisfy local conservation requirements, but we rather directly consider the conservative coupling between both schemes in the derivation to develop a novel concept suitable for implementation into finite element solvers based on piecewise linear shape functions.

We consider a class of applications which is concerned with a coupling between incompressible flow and transport equations. Our motivation is the study of large-scale geophysical phenomena such as mantle convection physics, which occur on a wide range of time and length scales, requiring long term simulations of large-scale coupled systems; cf. e.g. [14, 43, 46].

As a model problem, we choose a generalized Stokes-type problem, serving as a simplified variant of the more complex physics used in the simulation of convection in the Earth's mantle [43]. For simplicity, we use the Boussinesq approximation with constant conductivity, and we neglect inertia and internal heating. This results in the following set of non-dimensional balance equations, governing the conservation of momentum, mass and energy in a bounded domain $\Omega \subset \mathbb{R}^d, d = 2, 3$:

$$\begin{aligned} (1a) \quad & -\operatorname{div}(2\mu(\vartheta, z) \operatorname{sym}\nabla \mathbf{u}) + \nabla p = -\vartheta \hat{\mathbf{e}}, & \text{in } \Omega \times (0, t_{\text{end}}], t_{\text{end}} > 0, \\ (1b) \quad & \operatorname{div} \mathbf{u} = 0, & \text{in } \Omega \times (0, t_{\text{end}}], \\ (1c) \quad & \partial_t \vartheta + \operatorname{div}(\vartheta \mathbf{u} - \text{Ra}^{-1} \nabla \vartheta) = 0. & \text{in } \Omega \times (0, t_{\text{end}}]. \end{aligned}$$

Here \mathbf{u} represents the velocity field, p the pressure, ϑ the temperature, and $\hat{\mathbf{e}}(\mathbf{x})$ is the unit-length vector aligned with gravitational forces. The normalized viscosity μ potentially depends on the temperature ϑ and/or the depth $z(\mathbf{x})$ which is a domain-specific function of $\mathbf{x} := (x_1, \dots, x_d) \in \Omega$, and the Rayleigh-number $\text{Ra} > 0$ determines the presence and vigorosity of convection caused by the gravitational forcing term which is given by $-\vartheta \hat{\mathbf{e}}$. In mantle convection models, we typically deal with situations where $\text{Ra} \gg 1$ (a typical value for numerical models is $4.2 \cdot 10^7$), i.e., the energy transport is strongly dominated by convection [43].

To make the problem well-posed, we consider an initial temperature field $\vartheta(t = 0) = \vartheta^0$ and homogeneous Neumann boundary conditions $\text{Ra}^{-1} \nabla \vartheta \cdot \mathbf{n} = 0$ on the whole boundary $\partial\Omega$ of the computational domain, where \mathbf{n} denotes an outward-pointing unit-normal vector. For the Stokes part, we set no-slip Dirichlet-boundary conditions $\mathbf{u} = \mathbf{0}$, which obviously satisfy the compatibility condition $\int_{\partial\Omega} \mathbf{u} \cdot \mathbf{n} \, ds = 0$. The extension of the framework to more general boundary conditions is fairly straightforward and not considered here for the sake of brevity. We shall however present results obtained with other boundary type conditions when we discuss the numerical examples in Section 3.

Similarly structured models have applications in other fields where mass conservation is important, e.g., in ice sheet modeling [37, 42, 38], or in two-phase flow, where, instead of a temperature field, the evolution of an interface is considered in (1c); cf. e.g. [45, 40, 20, 33]. Although we consider only those physical effects here which are important for the following presentation, we would like to emphasize that the extension to more realistic situations involving for instance inertial terms and additional transport phenomena is possible. Using a suitable reformulation of the model equations in terms of the conservative momentum density $\rho \mathbf{u}$ instead of the velocity \mathbf{u} , we can also incorporate slight compressibility effects. This

allows the generalization of the approach proposed in this paper towards more sophisticated convection models such as the anelastic liquid approximation of mantle convection [43]. Similar ideas were previously proposed in the context of compressible flow [44].

The outline of this work is as follows: In the following Section 2, we shall introduce the necessary notation and the variational form of our conservative coupling strategy. We furthermore briefly discuss the extension to other stabilizations for the Stokes part of the problem and higher order time-integration schemes for the energy equation. Then in Section 3, we show a series of numerical results which are motivated by standard geophysical benchmarks. We demonstrate the performance of the novel coupled scheme in several examples by comparing it to a non-conservatively coupled scheme. Finally, in Appendix A, we discuss some details concerning the efficient implementation of the proposed approach in three-dimensional settings.

2. CONSERVATIVE COUPLING

In the following, we shall restrict ourselves to first-order explicit time-stepping for simplicity; extensions to higher order time-integration shall be discussed in Sect. 2.3. By approximating $\partial_t \vartheta \approx (\vartheta^{n+1} - \vartheta^n)/\Delta t^n$, we obtain a desirable decoupling of the problem into an instantaneous constraint given in form of a generalized Stokes equation

$$(2a) \quad -\operatorname{div}(2\mu(\vartheta^n, z) \operatorname{sym}(\nabla \mathbf{u}^n)) + \nabla p^n = -\vartheta^n \hat{\mathbf{e}}, \quad \text{in } \Omega,$$

$$(2b) \quad -\operatorname{div} \mathbf{u}^n = 0, \quad \text{in } \Omega,$$

and a semi-discretization of an equation of transport-type

$$(2c) \quad \vartheta^{n+1} = \vartheta^n - \Delta t^n \operatorname{div}(\vartheta^n \mathbf{u}^n - \text{Ra}^{-1} \nabla \vartheta^n) \quad \text{in } \Omega,$$

which can be solved by advancing the respective sub-problems in a time-stepping fashion for $n = 0, 1, \dots$. For this, we need to discretize the equations also spatially in a meaningful way. Due to their popularity in CFD codes and because of the simplicity of the underlying data-structures, we propose a discretization in terms of stabilized equal-order finite-elements for the flow part and vertex-centered finite-volumes for the transport. Before we discuss the discrete coupled scheme, let us introduce some necessary notation regarding the computational meshes.

2.1. Primal and dual mesh. Let us in the following assume that Ω is a d -polytope that is subdivided into d -simplicial *elements* to obtain a triangulation \mathcal{T}_h of our computational domain, satisfying the usual shape-regularity assumptions [16]. We shall refer to \mathcal{T}_h as the *primal* mesh. Based on this triangulation we construct a *dual* mesh as it is often done for finite-volume methods. To be precise, let $\mathcal{T}_i \subseteq \mathcal{T}_h$ denote the nodal patch associated with the vertex \mathbf{x}_i , $i = 1, \dots, N$, of the primal mesh, and let $\lambda_i^T(\mathbf{x})$ denote the barycentric coordinate of $\mathbf{x} \in \mathbb{R}^d$ with respect to the vertex \mathbf{x}_i belonging to any element $T \in \mathcal{T}_i$. We define

$$B_i^T := \{\mathbf{x} : \lambda_i^T(\mathbf{x}) \geq \lambda_j^T(\mathbf{x}), i \neq j\},$$

and we set $B_i := \bigcup_{T \in \mathcal{T}_i} B_i^T$. This construction results in a partition of Ω into d -polytopes B_i which we shall refer to as the set $\mathcal{B}_h := \{B_i, i = 1, \dots, N\}$ of *control volumes*. For an illustration of typical control volumes in $d = 2, 3$ dimensions, we refer to Figure 1.

The boundary ∂B_i of every such volume B_i can be decomposed into the set of internal control facets $\gamma_{ijk} = \partial B_i \cap \partial B_j \cap T_k : B_j \neq B_i$ and boundary facets $\gamma_{ik}^\partial = \partial \Omega \cap \partial B_i \cap \partial T_k$, where B_i and $B_j \in \mathcal{B}_h$ are the control volumes defined with respect to the two vertices \mathbf{x}_i and \mathbf{x}_j , which are both end points of an edge of some $T_k \in \mathcal{T}_h$. A more detailed description of the

barycentric dual meshes is given in [8, 35]. Details concerning the implementation in three dimensions are discussed in Appendix A.2.

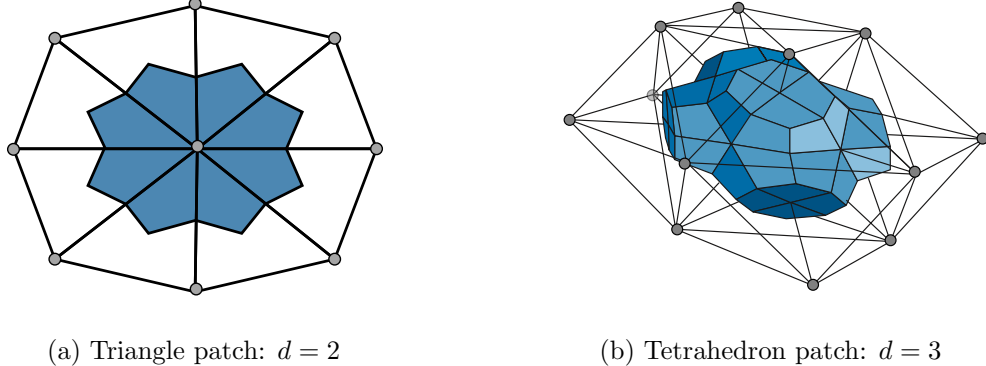


Figure 1. Illustration of a nodal patch \mathcal{T}_i around a vertex \mathbf{x}_i with the associated dual control volume B_i (shaded).

2.2. Coupling of finite elements and finite volumes. As the basic function space, we introduce the linear Lagrangian finite element space on the primal mesh \mathcal{T}_h , i.e.,

$$Q_h := \{ q_h \in H^1(\Omega), \quad q_h|_T \in P_1(T), \quad T \in \mathcal{T}_h \}.$$

For convenience, we also introduce finite-dimensional spaces satisfying zero boundary conditions for the velocity, i.e., $\mathbf{V}_h := [Q_h \cap H_0^1(\Omega)]^d$. Since our aim is to construct an **equal-order scheme**, we shall define all our other unknowns and coefficient functions formally as members of Q_h although the interpretation in the variational sense might differ. On the barycentric dual mesh, we define the space

$$R_h := \{ r_h \in L^2(\Omega), \quad r_h|_B \in P_0(B), \quad B \in \mathcal{B}_h \},$$

and due to the fact that $\dim R_h = \dim Q_h = N_Q$, we can define a natural bijection between these two spaces. More precisely, given the nodal basis ϕ_i of Q_h and the piecewise constant basis χ_i of R_h , we can define the natural transfer operators

$$\pi_h : \sum_{i=1}^{N_Q} q_i \chi_i \rightarrow \sum_{i=1}^{N_Q} q_i \phi_i, \quad \text{and} \quad \bar{\pi}_h : \sum_{i=1}^{N_Q} q_i \phi_i \rightarrow \sum_{i=1}^{N_Q} q_i \chi_i.$$

Note that $\pi_h \bar{\pi}_h = \bar{\pi}_h \pi_h = \text{id}$ holds by construction, which is a crucial property, since it ensures that the transfer between the meshes by itself cannot introduce unwanted damping effects as we would observe e.g. in averaging procedures.

The coupled algorithm is given as follows: For each $n = 1, 2, \dots$, we then first evaluate the nodal values of the viscosity coefficient $\mu_h^n \in Q_h$, and subsequently we consider the following stabilized weak formulation for discretizing the Stokes problem: find $(\mathbf{u}_h^n, p_h^n) \in \mathbf{V}_h \times Q_h / \mathbb{R}$ such that

$$(3) \quad \begin{aligned} & \int_{\Omega} 2\mu_h^n \operatorname{sym} \nabla \mathbf{u}_h^n : \nabla \mathbf{v}_h \, d\mathbf{x} - \int_{\Omega} p_h^n \operatorname{div} \mathbf{v}_h \, d\mathbf{x} \\ & - \int_{\Omega} \operatorname{div} \mathbf{u}_h^n \cdot q_h \, d\mathbf{x} - \sum_{T \in \mathcal{T}_h} \int_T \alpha \nabla p_h^n \cdot \nabla q_h \, d\mathbf{x} = - \int_{\Omega} \vartheta_h^n \hat{\mathbf{e}} \cdot \mathbf{v}_h \, d\mathbf{x}, \end{aligned}$$

for all test functions $(\mathbf{v}_h, q_h) \in \mathbf{V}_h \times Q_h$. The element-wise defined stabilization function α needs to be chosen suitably for stability. Below we consider the stabilization due to Brezzi and Pitkäranta [13] where $\alpha|_T := c_T \operatorname{diam}(T)^2 / \bar{\mu}_T^n$ for some sufficiently large constant $c_T > 0$, and $\bar{\mu}_T^n := |T|^{-1} \int_T \mu_h^n \, d\mathbf{x}$ denotes the element-wise average of the viscosity.

Based on the discrete velocity solution, the transport equation for the temperature is then advanced by an upwind finite-volume scheme. The variational form can be written as a Petrov-Galerkin scheme of the following form: given $(\mathbf{u}_h^n, p_h^n) \in \mathbf{V}_h \times Q_h$ and $\vartheta_h^n \in Q_h$, find $\vartheta_h^{n+1} \in Q_h$ such that

$$(4) \quad \sum_{B_i \in \mathcal{B}_h} \int_{B_i} \bar{\pi}_h \vartheta_h^{n+1} r_h \, d\mathbf{x} = \sum_{B_i \in \mathcal{B}_h} \int_{B_i} \vartheta_h^n r_h \, d\mathbf{x} - \Delta t_n \mathcal{A}(\vartheta_h^n, r_h),$$

for all $r_h \in R_h$, where the use of $\bar{\pi}_h$ introduces a mass-lumping and we define the bilinear form

$$\mathcal{A}(\vartheta_h^n, r_h) := \sum_{B_i \in \mathcal{B}_h} \int_{\partial B_i \setminus \partial \Omega} (\mathbf{j}(\mathbf{u}_h^n, p_h^n) \langle \vartheta_h^n \rangle_{\text{up}} - \text{Ra}^{-1} \nabla \vartheta_h^n \cdot \mathbf{n}_i) r_h \, ds,$$

where \mathbf{n}_i is the unit normal vector pointing outward of B_i . For consistency, $\mathbf{j}(\mathbf{u}_h^n, p_h^n)|_{\partial B_i}$ should be an approximation of the normal velocity component $\mathbf{u}(t^n)|_{\partial B_i} \cdot \mathbf{n}_i$, and $\langle \vartheta_h^n \rangle_{\text{up}}$ denotes the upwind value, which is piecewise defined for any control facet γ_{ijk} . Given the net flux $J_{ijk} := \int_{\gamma_{ijk}} \mathbf{j}(\mathbf{u}_h^n, p_h^n)|_{\partial B_i} \, ds$, we define

$$\langle \vartheta_h^n \rangle_{\text{up}}|_{\partial B_i \cap \gamma_{ijk}} := \begin{cases} \vartheta_h^n|_{B_i} & \text{if } J_{ijk} \geq 0 \\ \vartheta_h^n|_{B_j} & \text{if } J_{ijk} \leq 0 \end{cases}, \quad i \neq j.$$

A simple and consistent choice for the flux $\mathbf{j}(\mathbf{u}_h^n, p_h^n)|_{\partial B_i}$ would be $\mathbf{u}_h^n|_{\partial B_i} \cdot \mathbf{n}_i$. However, for a discrete solution obtained by (3), we cannot expect this velocity field to be locally conservative. Hence, we propose a flux that is capable of eliminating the compressibility effects introduced by the stabilization. It reads as

$$(5) \quad \mathbf{j}(\mathbf{u}_h^n, p_h^n)|_{\partial B_i} := (\mathbf{u}_h^n - \alpha \nabla p_h^n)|_{\partial B_i} \cdot \mathbf{n}_i.$$

This flux has two important properties: Firstly, like $\mathbf{u}_h^n|_{\partial B_i} \cdot \mathbf{n}_i$ it is single-valued and directed on the control facets γ_{ijk} , i.e., there holds that $\mathbf{j}(\mathbf{u}_h^n, p_h^n)|_{\partial B_i \cap \gamma_{ij}} = -\mathbf{j}(\mathbf{u}_h^n, p_h^n)|_{\partial B_j \cap \gamma_{ij}}$. Secondly, it is conservative in the sense that the integral $\int_{\partial B_i} \mathbf{j}(\mathbf{u}_h^n, p_h^n) \, ds$ vanishes if (\mathbf{u}_h^n, p_h^n) solve the system (3); cf. [30, Theorem 3.2, Lemma 4.1] for a formal proof. By this we make sure that local conservation in a discrete sense is ensured, even though our discrete velocities may not strongly satisfy $\operatorname{div} \mathbf{u}_h^n = 0$.

Remark 2.1. If the corrected flux $\mathbf{j}(\mathbf{u}_h^n, p_h^n)$ is conservative with respect to the control volumes, it is easy to show that the convective part of the operator corresponding to $\mathcal{A}(\cdot, \cdot)$ has a vanishing row and column sum. Using the arguments of [9, Lemma 4.5] we can conclude that the convective part of the discrete operator is positive-semidefinite. Hence, combined with a diffusion- and/or reaction-type term, the transport part of the coupled scheme is also stable, which is in contrast to the scheme without correction, for which this property is not guaranteed. As we shall see in the numerical results of Section 3 critical overshoots can occur if we use the non-conservative flux $\mathbf{u}_h^n|_{\partial B_i} \cdot \mathbf{n}_i$.

Remark 2.2. The mass-corrected coupling approach can be extended to other choices of pressure stabilizations. For instance, the stabilized equal-order method due to Bochev et al. [11] amounts to choosing a tensorial parameter function $\alpha|_T := (\bar{\mu}_T^n)^{-1} \int_T (\mathbf{x} - \mathbf{x}_T)(\mathbf{x} - \mathbf{x}_T)^\top \, d\mathbf{x}$, where \mathbf{x}_T

denotes the barycenter of T . For other types of stabilization the form of the conservative flux (5) may be different, but it can be derived in a systematic fashion as shown in [30].

Remark 2.3. The extension of these ideas to higher order elements with continuous pressure spaces is possible. However, since this typically results in mixed finite elements and opens the question of matching transport schemes, we restrict ourselves to the lowest-order case, where the coefficients of every component can be stored within the same lean data-structures. In practical implementations this restriction has been demonstrated to achieve an excellent performance and parallel scalability with up to $\mathcal{O}(10^{12})$ unknowns; cf. the discussion in [29, 28]. For the discussion of higher order flux corrections, we refer the interested reader to [30].

2.3. Higher order time-stepping. The approach described above is clearly not limited to first-order explicit time-stepping and a variety of explicit and (semi-)implicit approaches could be considered, e.g., the ones considered in [36, 15] for mantle convection. Such approaches have in common that they introduce a velocity splitting between the Stokes part of the problem and the energy equation, since the solution of a fully coupled nonlinear system once per time-step is often not feasible. Moreover, due to the different character of the sub-problems, the coupling may for some applications be relaxed in such a way that the Stokes problem is considered with a different order in the temporal integration.

In the following, we would like to discuss a strongly stability preserving (SSP) Runge-Kutta scheme [31], which consists of a combination of two explicit-Euler steps and thereby inherits the stability properties of this method. For convenience, let us define $\mathcal{L}\vartheta := \operatorname{div}(\vartheta \mathbf{u} - \text{Ra}^{-1} \nabla \vartheta)$ and assume that \mathbf{u} is known. Given an approximation ϑ^n of the temperature at time t_n , one step of the second order two-stage scheme SSP(2,2) for determining an approximation of the temperature field ϑ^{n+1} at time $t_n + \Delta t_n$ consists of the following sub-steps [31]:

$$(6a) \quad \vartheta^{(1)} = \vartheta^n + \Delta t_n \mathcal{L}\vartheta^n,$$

$$(6b) \quad \vartheta^{(2)} = \vartheta^{(1)} + \Delta t_n \mathcal{L}\vartheta^{(1)},$$

$$(6c) \quad \vartheta^{n+1} = \frac{1}{2}(\vartheta^n + \vartheta^{(2)}).$$

Hence, in a fully-discrete scheme, the discrete variant of \mathcal{L} is applied two times, where for the step (6b) one would already need an approximation of the velocity \mathbf{u} at time t_{n+1} which requires an extra solve of the saddle-point system (3). Since this implicit solve usually constitutes the most expensive part of the time-stepping, and since the temporal behavior of both subproblems in the model problem (1) differs (the time-derivative in the mass and momentum balance is considered negligible), we introduce an explicit splitting of first order to avoid excessive computations of the velocity field. Similar to [15], we propose updating the velocity only once between steps (6a) and (6b), i.e., \mathbf{u}^{n+1} is determined by $\vartheta^{(1)}$. Thus, compared to the explicit Euler algorithm, the computation of each time-step in the improved SPP scheme only involves a second evaluation of the discrete transport operator. The extra cost for this is comparably small to the overall effort and can thus be justified by the expected higher temporal accuracy that the scheme can attain in situations where the evolution of the temperature field is more vigorous than that of the velocity field.

3. NUMERICAL EXAMPLES

In this section, we show some numerical experiments that demonstrate the importance of locally conservative flow-transport couplings in simplified examples that resemble flow situations occurring in geophysical research. Finally, we address the issue of iterative solvers

and show large-scale results. If not mentioned otherwise, we use the SPP(2,2) time-stepping with a first order velocity splitting as described in Section 2.3. The time steps are always chosen small enough to obey the CFL stability condition.

3.1. Differentially heated cavity. For our first example, we consider a natural convection problem at infinite Prandtl number in $\Omega := (0, 1)^d$, $d = 2, 3$, with no-slip conditions $\mathbf{u} = \mathbf{0}$ on the whole boundary $\partial\Omega$. On the left boundary, we apply a heating $\vartheta|_{x_1=0} = 1$ and on the right hand side, we apply a cooling $\vartheta|_{x_1=1} = 0$, while the remaining boundaries are insulated, i.e., $\nabla\vartheta \cdot \mathbf{n}|_{x_i=0} = \nabla\vartheta \cdot \mathbf{n}|_{x_i=1} = 0$, $i = 2, \dots, d$. Moreover, gravity acts in direction $\hat{\mathbf{e}} := (0, \dots, -1)^\top$ and the viscosity $\mu = 1$ is constant. We consider a Rayleigh-number of $\text{Ra} = 10^6$ for which it is known that a steady state solution exists.

As pointed out by Galvin et. al. [24], this so-called *differentially heated cavity problem* is particularly challenging for standard conforming finite elements, since weakly divergence-free functions are in most cases not divergence-free, which may cause problems in simulations where flow is coupled to transport. As it is often not feasible to excessively increase the resolution of the mesh, and thereby decrease the spurious effects arising from weak incompressibility in finite-dimensional function spaces, they propose using either strongly divergence-free finite element formulations or suppress the divergence of the flow-field by penalization to obtain better results. To demonstrate that also a weak mass balance without additional penalization is sufficient to obtain qualitatively good results in such coupled simulations, we conduct a series of numerical experiments:

In Figure 2, we show the steady state solutions obtained in a refinement study for the two-dimensional heated cavity example with and without conservative fluxes. For the initial triangulation we use a triangular cross-mesh which result from the insertion of cell midpoints in an $m \times m$ lattice, and we refine two layers of elements near the boundary where we expect the highest gradients. We observe that the proposed scheme with flux-correction converges to a steady state solution which agrees well with the results obtained by a higher-order method in [18]. The uncorrected approach however has problems to converge near the upper boundary, where solution overshoots of up to two orders of magnitude can be observed for the coarsest mesh. These problems vanish in the limit $h \rightarrow 0$ as our refinement study indicates. However, at least for this example we see already by visual inspection that the rate with which these effects decay renders the uncorrected approach impractical, especially if we consider higher Rayleigh numbers.

To validate our three-dimensional implementation in the hierarchical hybrid grid framework (HHG, [3]), we also conduct an experiment on a uniform mesh consisting of 6 291 456 tetrahedral elements. We compare the solution in the middle-plane $x_2 = 0.5$ to the two-dimensional reference solution. It can be observed that in the three-dimensional case the over- and undershoots are less severe than in the two-dimensional cases, i.e., they typically stay below 5% even for coarser meshes. However, as Figure 3 indicates, the uncorrected scheme still shows a much larger deviation from the reference solution than the method with flux-correction. More computational results and details on the solver will be presented in Section 3.4.2.

3.2. Depth- and temperature-dependent viscosity models. In this test, we simulate a first geophysically motivated problem similar to case 2 in Blankenbach et. al. [10]. We consider the system of equations (1) in $\Omega = (0, 1)^2$ with free-slip boundary conditions for the velocity, i.e., $\mathbf{u} \cdot \mathbf{n} = \mathbf{t}^\top (\text{sym } \nabla \mathbf{u}) \cdot \mathbf{n} = 0$, where \mathbf{t} is a tangential vector on $\partial\Omega$. For the temperature

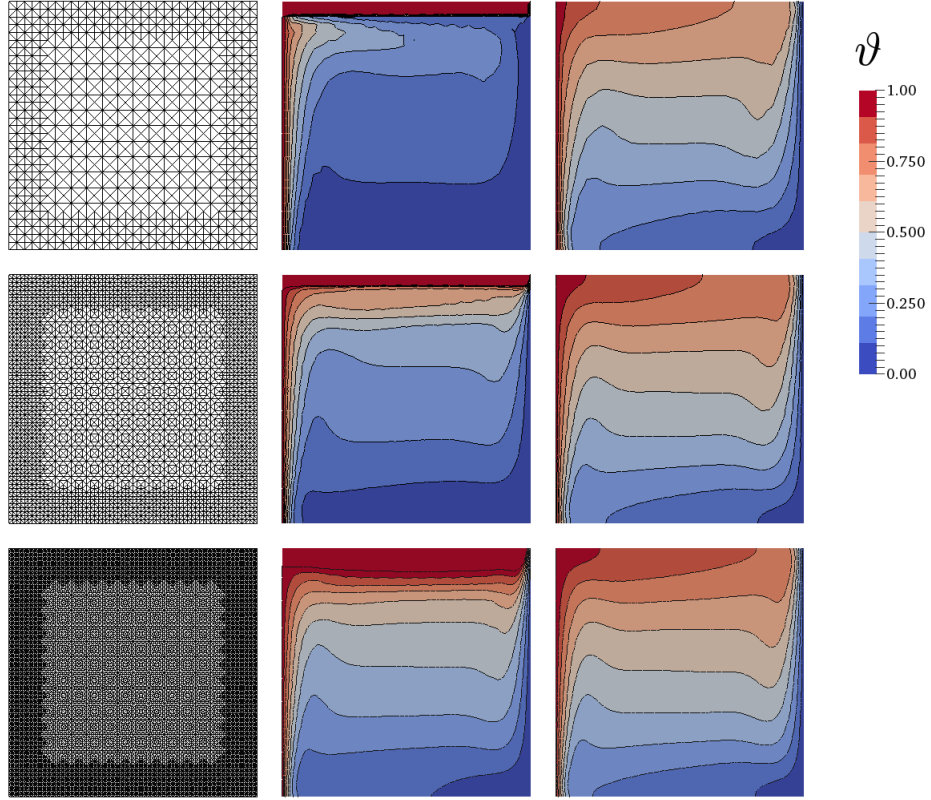


Figure 2. Meshes (left) and steady state solution for the differentially heated cavity example at $\text{Ra} = 10^6$ for the uncorrected (center) and corrected (right) scheme. From top to bottom we show meshes with $m \in \{16, 32, 64\}$.

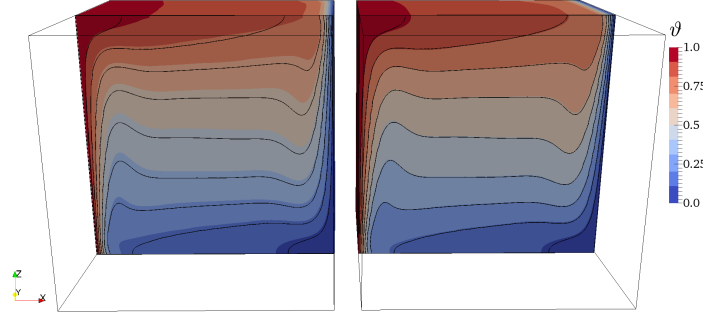


Figure 3. Steady state solution for the three-dimensional differentially heated cavity example at $\text{Ra} = 10^6$ for the uncorrected (left) and corrected (right) scheme. We clip the volume plot at $x_2 = 0.5$ and superimpose the corresponding contour lines (black) of the two-dimensional reference solution ($m = 64$).

we apply a heating at the bottom $\vartheta|_{x_2=0} = 1$ and a cooling at the top $\vartheta|_{x_2=1} = 0$, while the remaining boundaries are insulated, i.e., $\nabla\vartheta \cdot \mathbf{n}|_{x_1=0} = \nabla\vartheta \cdot \mathbf{n}|_{x_1=1} = 0$. Moreover, we initially

prescribe a smoothly perturbed temperature gradient

$$\vartheta^0(\mathbf{x}) = 1 - x_2^2 + \varepsilon \cos(k\pi x_1) \sin(2\pi x_2).$$

with $k = 4$ and $\varepsilon = 0.01$. The gravitation acts in direction $\hat{\mathbf{e}} := [0, -1]^\top$ and the viscosity model may be chosen as both, depth and temperature dependent, i.e.,

$$(7) \quad \mu(\vartheta, z) = \exp(-b\vartheta + cz),$$

where the depth is defined as $z = 1 - x_2$.

In our first test, we take the values of case 2(a) in [10], i.e., we set $b = \ln(1000)$, $c = 0$ and $\text{Ra} = 10^4$. We conduct a mesh-refinement study to demonstrate the curing effect of the mass-correction. For this, we again take $m \times m$ triangular cross-meshes, which have the advantage that they are symmetric with respect to both coordinate axes and thereby avoid the deterioration of symmetry in the numerical solutions due to mesh-effects. Moreover, to capture the physics in the boundary layers better, we refine two layers of elements at the top and bottom borders of the initial mesh.

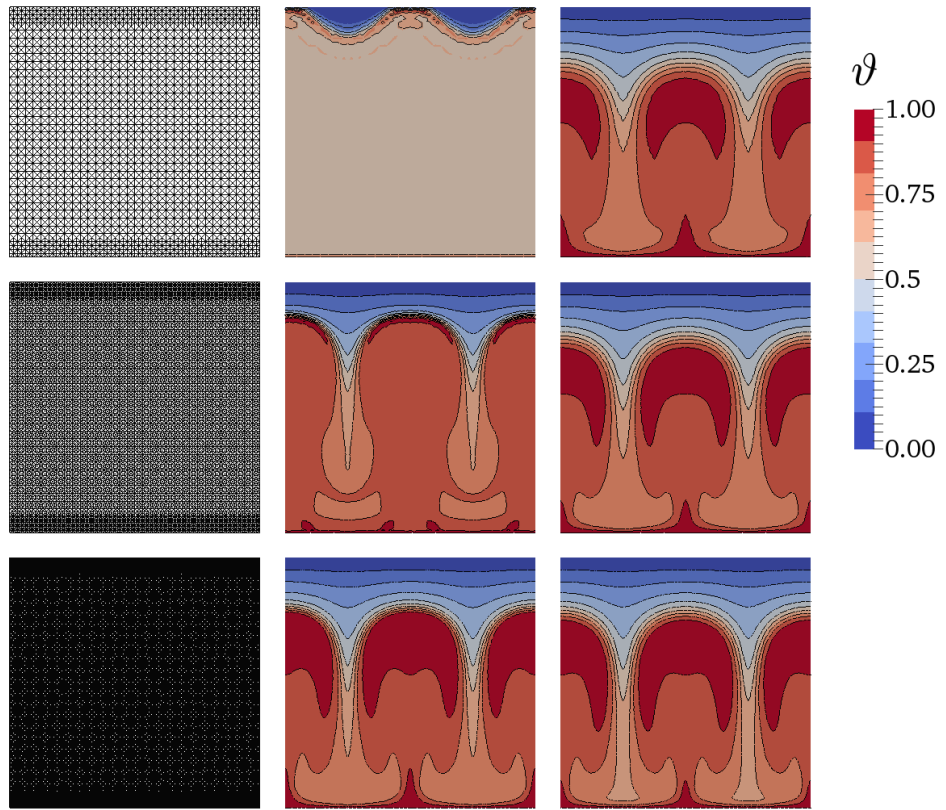


Figure 4. Temperature solution at $t = 10$ for $\text{Ra} = 10^4$ in the fully coupled test 2(a) with a temperature-dependent viscosity. Meshes (left) and solutions for the uncorrected scheme (center; normalized to range $[0, 1]$) and the corrected scheme (right) for $m \in \{32, 64, 128\}$ divisions in each direction (from top to bottom).

In Figure 4, we depict the results at the non-dimensional time $t = 10$ for a series of meshes with increasing resolution $m \in \{32, 64, 128\}$. It can be clearly observed that the

coupled method without mass-correction is not capable of solving the problem at lower mesh resolutions, while the corrected approach shows smooth temperature solutions even at coarser levels. Moreover, while for the coarser levels the amount of detail is clearly limited by the resolution, the corrected approach captures the evolutionary behavior of the solution much better.

In a second test, we take both a temperature- and depth-dependent viscosity, i.e., as in case 2(b) in [10], i.e., we set $b = \ln(16384)$ and $c = \ln(64)$ and $\text{Ra} = 10^4$. Again, we consider the series of meshes constructed as above for $m \in \{32, 64, 128\}$ and compare the uncorrected approach to the corrected one. In Figure 5, we depict the results at $t = 10$.

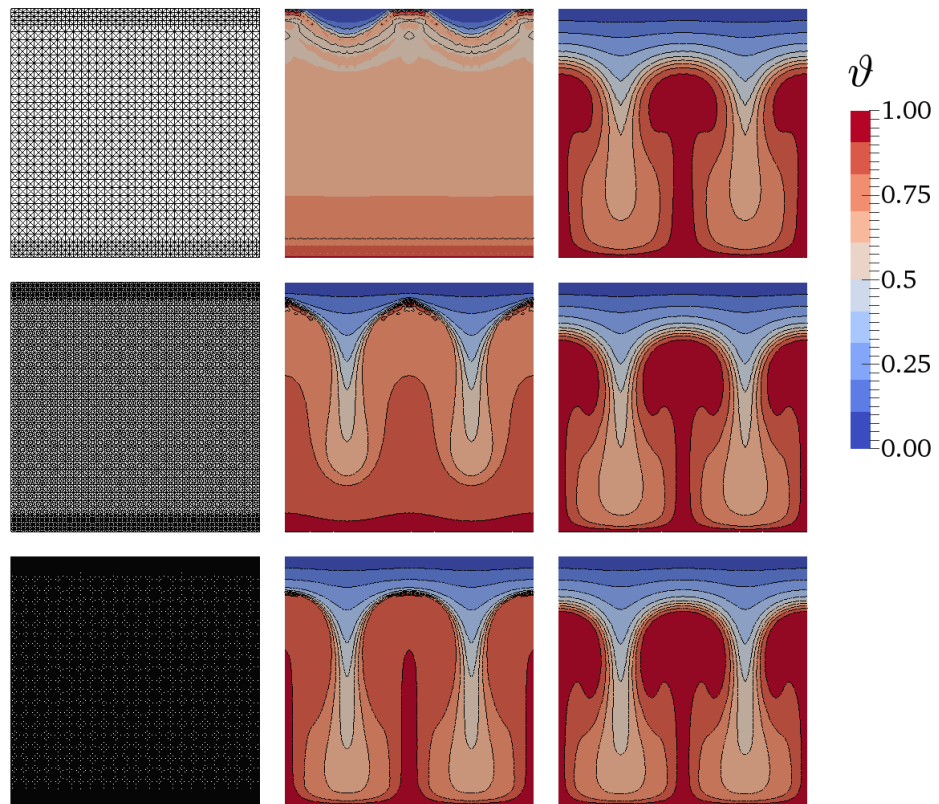


Figure 5. Temperature solution at $t = 10$ for $\text{Ra} = 10^4$ in the fully coupled test 2(b) with a temperature- and depth-dependent viscosity. Meshes (left) and solutions for the uncorrected scheme (center; normalized to range $[0, 1]$) and the corrected scheme (right) for $m \in \{32, 64, 128\}$ divisions in each direction (from top to bottom).

Again, it can be observed that the coupled method without mass-correction is not remotely capable of solving the problem with reasonable mesh resolutions. Here due to the stronger nonlinearities the effect is even more severe. We suspect that 1-2 more refinement levels would be required to obtain a solution with the uncorrected approach that is qualitatively comparable to the solution obtained with corrected fluxes.

To show the severeness of the long-term effects, we conduct a long term simulation for the two finer resolutions $m \in \{64, 128\}$ and make a temporal plot of two quantities which are

often reported in geophysical publications, namely the Nusselt number

$$\text{Nu} := -\frac{\int_0^1 \partial_{x_2} \vartheta|_{x_2=1} ds}{\int_0^1 \vartheta|_{x_2=0} ds}$$

(i.e. the ratio of the mean surface temperature gradient over the mean bottom temperature) and the root-mean-square (rms) velocity $\text{rms}(\mathbf{u}) := |\Omega|^{-1/2} \|\mathbf{u}\|_{L^2(\Omega)}$. In the results which are depicted in Figure 6, it can be seen that the corrected approach produces essentially the same behavior for both resolutions while the uncorrected approach manifests a significant mesh-dependency. It can also be observed that the uncorrected solution approaches a similar behavior as the corrected scheme for increasing resolutions. However, even for the finest mesh the Nusselt numbers still deviate substantially while the root-mean-square velocity better matches the characteristics of the solution obtained by the corrected scheme.

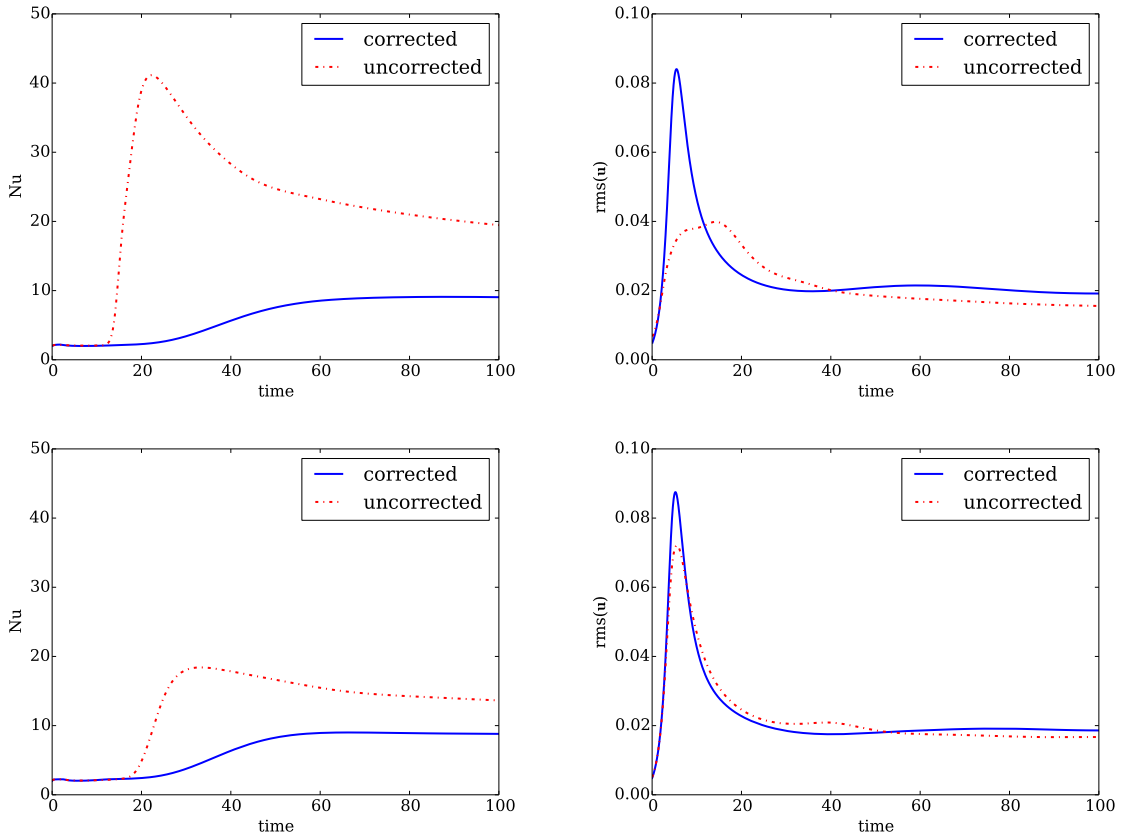


Figure 6. Nusselt numbers and root mean square velocities for the fully coupled test 2(b) with a temperature- and depth-dependent viscosity. The resolutions are $m = 64$ for the top results and $m = 128$ for the results at the bottom.

3.3. Inexact solvers. From (5) it is obvious that the fluxes can be explicitly computed based on any approximation $(\tilde{\mathbf{u}}_h, \tilde{p}_h) \in \mathbf{V}_h \times Q_h$ regardless of the closeness of the discrete approximation to the true discrete solution (\mathbf{u}_h, p_h) of the variational problem (3). So for a practical implementation, there is nothing that prevents us from relaxing the assumption

of exact solutions. However, if we revisit the construction in [30], we find that the exact conservativeness of the corrected fluxes relies on the assumption that the weak mass-balance of the Stokes sub-problem (3) is satisfied exactly. In practice, this will be violated, e.g. when an iterative solver is stopped after reaching a finite precision. Especially in transient computations it may be prohibitively expensive to solve for full accuracy in each time step.

The question whether the corrections can improve the quality of discrete solutions, even if an exact discrete solution is not available, is addressed in the following experiment. This is done by solving only approximately and studying the temperature-fluctuations of the approximate discrete solution of the problem

$$\begin{aligned} -\Delta \mathbf{u} + \nabla p &= -\tilde{\vartheta} \hat{\mathbf{e}}, \\ \operatorname{div} \mathbf{u} &= 0, \\ \partial_t \vartheta + \mathbf{u} \cdot \nabla \vartheta &= 0, \end{aligned}$$

in $\Omega := (0, 1)^3$ for $t \in (0, t_{\text{end}}]$, $t_{\text{end}} > 0$, where we again prescribe free-slip boundary conditions for the velocity. The above problem can be seen as a constant viscosity variant of the generalized Stokes model (1) in the hyperbolic limit $\text{Ra} \rightarrow \infty$, where the temperature becomes a purely advected and conserved quantity in Ω .

To obtain only a one-way coupling, where we have no back-coupling of the temperature to the flow field, we further replaced ϑ in the right hand side of the Stokes part by a known temperature field $\tilde{\vartheta}(\mathbf{x}) := \cos(2\pi x_1) \cos(2\pi x_2) \sin(\pi x_3)$, which induces a forcing in the gravitational direction $\hat{\mathbf{e}} := (0, 0, -1)^\top$. The temperature field is initialized with the exact solution $\vartheta(t) = 1$ which should remain constant for all times due to the absence of source terms. Since the coupled scheme is zeroth-order consistent in the sense of [19], the constant is preserved during the advection, given that the discrete Stokes solution exactly satisfies the weak incompressibility constraint [30]. However, instead of using an exact discrete solution, we compute the solution of the discrete Stokes equations by a preconditioned Krylov subspace method up to a relative tolerance `rtol` and use this discrete velocity in the coupled scheme to convect the temperature field until $t_{\text{end}} = 100$. For the Krylov solver, we use a transpose free quasi minimal residual scheme (TFQMR, available from the PETSc toolkit, [23, 1]) together with an algebraic multigrid based (using ML-AMG, [25]) block-diagonal preconditioner consisting of a discrete vector-Laplacian for the velocity and a mass matrix for the pressure Schur-complement; cf. [21] for details. In our experiments, we set the absolute tolerance (i.e., the absolute size of the preconditioned residual norm) to `atol` = 10^{-20} and vary the relative tolerance `rto1` (i.e., the relative decrease in the preconditioned residual norm) from 10^{-1} to 10^{-15} .

The intuition is that due to the inexact solves, we shall observe compressibility effects, resulting in a lack of zeroth order consistency. This is indeed the case as can be seen in Table 1, where we list the L^2 -errors $E_{\text{rtol}} := \|\vartheta(t_{\text{end}}) - \vartheta_h(t_{\text{end}})\|_{L^2(\Omega)}$, of the series of computations on a uniformly structured mesh with 196 608 tetrahedral elements. However, while the conservation of the approximate fluxes is clearly not exact for the given example, we notice a beneficial effect of the correction already before the discrete solution has reached an accuracy of two significant digits in the L^2 norm. We observe that while the consistency error for the transport without correction depends on the discretization error of the Stokes problem, the consistency error for the corrected transport depends only on the iteration error.

3.4. Convection in a spherical shell. As a motivation for future mantle convection models, we apply the conservatively coupled scheme to a buoyancy-driven flow problem in a spherical

r_{tol}	#it	residual	$E_{r_{tol}}$	$E_{r_{tol}}$ (corr.)
10^{-1}	2	6.442255e-04	3.973277e-02	1.890789e-02
10^{-2}	3	3.030742e-04	2.031140e-02	3.811628e-03
10^{-3}	9	2.940274e-07	1.880739e-02	1.754112e-06
10^{-6}	9	6.921875e-09	1.880776e-02	5.363015e-08
10^{-9}	15	1.442048e-11	1.880775e-02	1.040908e-10
10^{-12}	18	1.044333e-14	1.880775e-02	6.452550e-14
10^{-15}	22	4.597808e-17	1.880775e-02	2.114510e-15

Table 1. Relation of the (unpreconditioned) Stokes residual norm to the defect due to compressibility introduced by inexact TFQMR solves on a uniformly structured mesh with 196,608 tetrahedral elements.

shell, i.e., the region between two concentric spheres of different radii. We consider the problem (1) in a space-time domain $\Omega \times [0, t_{end}]$, where $\Omega := \{ \mathbf{x} \in \Omega : r_{\min} \leq |\mathbf{x}| \leq r_{\max} \}$ is the spherical shell domain with radii $r_{\min} = 0.55$ and $r_{\max} = 1$. Moreover, the gravity unit vector pointing to the center of the sphere is given by $\hat{\mathbf{e}}(\mathbf{x}) := -\mathbf{x}/|\mathbf{x}|$. For the initial conditions $\vartheta(t = 0) = \vartheta^0$, we choose an interpolation between the core and the surface temperature, where we add a spherical harmonic perturbation at mid-depth. In spherical coordinates, the initial condition is given by

$$(8) \quad \vartheta^0(r, \phi, \theta) := \frac{r_{\min}(r_{\max} - r)}{r(r_{\max} - r_{\min})} + \varepsilon \sin\left(\frac{\pi(r - r_{\min})}{r_{\max} - r_{\min}}\right) (\sin(2\phi) + \cos(2\phi)) \Phi(\theta),$$

where the perturbation magnitude is set to $\varepsilon = 0.01$, and $\Phi(\theta) = \sqrt{6.5625/\pi} \cos \theta \sin^2 \theta$ is a normalized associated Legendre polynomial of degree 3 and order 2 as described in [49]. The boundary conditions for the temperature are set to $\vartheta = 1$ at the core mantle boundary (i.e., at $r = 0.55$) and $\vartheta = 0$ at the surface ($r = 1$).

To obtain a grid for the spherical shell, we use a construction due to Baumgardner [2]: The initial step is the triangulation of the boundaries, for which we map the twelve vertices of a regular icosahedron onto a sphere. By connecting these vertices by thirty geodesic arcs, we obtain a mesh consisting of twenty equal spherical triangles. Recursively applying a dyadic midpoint refinement in terms of geodesic arcs, then allows us to generate surface meshes with the desired resolution. This triangulation immediately induces a quasi-uniform discretization of the shell-volume with prismatic elements organized in radial layers. In the last step, we refine the prismatic mesh into a nested hierarchy of conforming tetrahedral meshes; cf. Fig. 7 (left) for an illustration.

3.4.1. Tetrahedral symmetric convection pattern. In this example, we consider an isoviscous model and use a Nitsche-type method due to Freund and Stenberg [22] to prescribe free-slip boundary conditions on the whole boundary $\partial\Omega$. Similar to the setup considered e.g. in [47, 49, 15] we set the Rayleigh-number to $\text{Ra} = 7.7 \cdot 10^4$ and solve the instationary problem on a quasi-uniform partition of the spherical shell into 245 760 tetrahedral elements. We compute solutions with and without flux correction until the latter computation converges to a steady state solution, which is a tetrahedral symmetric convection pattern as depicted in Figure 7 (right) or – for reference – in [47, Figure 6.10]. We observe that the corrected scheme can produce the expected pattern, while the uncorrected scheme produces temperature ridges between the plume structures and hence is not capable to fully capture the long-term behavior of the system. For higher resolutions and nonlinear models, these effects may not manifest

themselves so obviously, but they can amplify over long periods of time and result in physically wrong solutions.

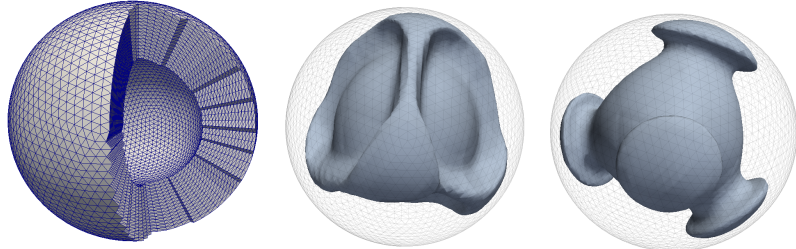


Figure 7. Uncorrected (center) vs. corrected (right) coupling approach: Contour surfaces $\vartheta = 0.4$ for the steady state temperature field for isoviscous Boussinesq flow with free-slip conditions and a Rayleigh-number of $Ra = 7.7 \cdot 10^4$.

3.4.2. Large scale example. In this example, we choose a slightly temperature-dependent viscosity model $\mu(\theta) := \exp(\frac{1}{2} - \theta)$ and we set no-slip conditions on the whole boundary. We further set $Ra = 10^7$ and the initial temperature field as well as the boundary conditions are prescribed by $\vartheta^0(r, 16\phi, 16\theta)$ which is again an interpolation between the core and the surface temperature with a perturbation of higher frequency than the previous example.

The computational mesh is again an icosahedral sphere mesh consisting of roughly a hundred million (94 371 840) individual tetrahedra and the discretization of the model problem (1) consists of 77 824 950 degrees of freedom in each time-step.

We solve the coupled problem with flux-correction for 10 000 time steps on a mid-sized department cluster consisting of 8 compute nodes connected by a QDR Infiniband network. Each node is equipped with 4 Intel Xeon E7-4830 CPUs (8 cores each) and 256 GB RAM. The Stokes problems are solved approximately by a conjugate gradient – geometric multigrid approach as described in [48, 28, 29], where we slightly shift some nodes in the multigrid hierarchy to better approximate the curved boundary $\partial\Omega$ of the spherical shell. For the initial solve of the Stokes system we conduct 20 PCG iterations and in every subsequent solve, we apply 8 steps of a preconditioned conjugate gradient (PCG) method to the pressure Schur-complement problem and approximate the inverse of the viscous operator by a $V(3, 3)$ cycle of the hierarchical hybrid grid (HHG) solver [3]. The PCG method is preconditioned by a lumped mass matrix which is scaled by the reciprocal viscosity as described in [32], and we restart the method every 4 iterations due to the inexactness of the Krylov space which is built up with respect to the approximate Schur-complement [48].

In Figure 8, we depict the solution of the temperature field for the corrected flux approach. Here we can clearly observe the characteristic formation of mushroom-shaped plumes that evolve from small perturbations. It should moreover be noted that the computed temperature fields obey a discrete maximum principle at all times during the simulation, which is in line with the physics of the underlying convection problem in the absence of internal heat sources.

4. CONCLUSION

We proposed a novel finite-element – finite-volume strategy for coupled flow and transport problems, which exactly conserves transported quantities and which can be efficiently implemented with lean data structures that produce minimal logistic overhead. The effectiveness

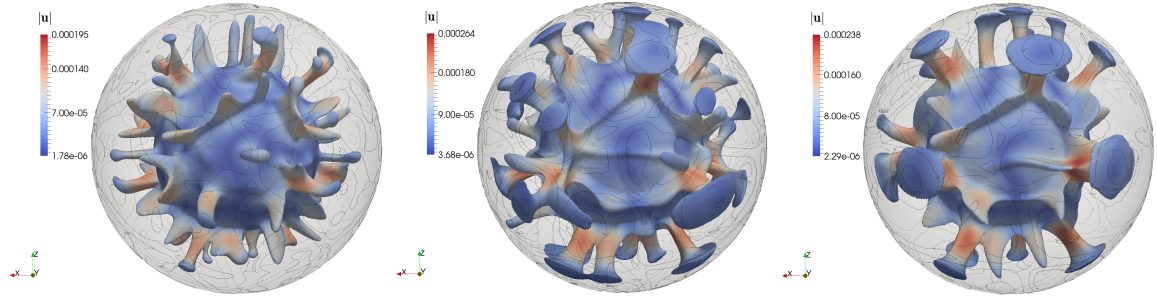


Figure 8. Isosurfaces for $\vartheta = 0.4$ colored by the velocity magnitude after 6 000, 8 000 and 10 000 timesteps (from left to right).

of conservative flux-corrections was demonstrated in a series of numerical examples in two and three space dimensions. In particular in combination with high Rayleigh numbers and strongly nonlinear viscosity models, we demonstrated that conservative couplings are crucial for obtaining physically meaningful results with resolutions that lend themselves to practical computation. In this respect, we have demonstrated how a long-standing deficiency of the piecewise linear finite element method can be circumvented in an elegant and inexpensive fashion. With the application of realistic large-scale computing in mind, we investigated the sensitivity of the proposed approach with respect to inexact solves, and we demonstrated large-scale results obtained by using the **parallel geometric multigrid implementation HHG** on a mid-sized department cluster. Although the model discussed in this paper is still too simplistic to be applied to state of the art geophysical research, the presented examples prove that the conservatively coupled discretization scheme can provide an important building block for massively parallel solvers for nonlinearly coupled flow-transport problems.

APPENDIX A. IMPLEMENTATION

To provide interested readers with the necessary information to implement the approach into their own codes, we outline here essential aspects for the implementation of the proposed coupling concept in a standard finite element code. Since the three-dimensional case is the most technically involved, we shall not elaborate on the two-dimensional case which follows by similar arguments. Moreover, since our parallel implementation employs a geometric multigrid solver based on the hierarchical hybrid grid (HHG) approach, we comment on potential savings in computational effort that can be exploited when using a matrix-free/stencil-based representation of the discretization on structurally refined meshes. For further details on the HHG framework we refer to [4, 6, 5, 27, 26].

A.1. Efficient assembly of variable-viscosity stencils. Let us consider the stiffness matrix for the viscous operator. The local stiffness matrix for the variable viscosity operator corresponds to the tensor $A_{\mu,T}^{k,l,i,j}$, where $k, l = 1, \dots, 3$ denote the velocity components and $i, j = 1, \dots, 4$ the nodal coefficients in the tetrahedron T defined by the vertices \mathbf{x}_i , $i = 0, \dots, 3$. Its entries are computed as

$$A_{\mu,T}^{i,j,k,l} = \int_T \mu_h (\partial_{x_k} \phi_i^T \cdot \partial_{x_l} \phi_j^T + \delta_{kl} \nabla \phi_i^T \cdot \nabla \phi_j^T) \, d\mathbf{x},$$

where ϕ_i^T are the nodal shape functions associated with the element T . For linear tetrahedral finite elements, the gradients of the shape functions are constant, which allows us to factor out

$\bar{\mu}_T := |T|^{-1} \int_T \mu_h \, d\mathbf{x}$. For coefficients defined with respect to a linear nodal basis this further simplifies to $\bar{\mu}_T = \frac{1}{4} \sum_{i=1}^4 \mu_h(\mathbf{x}_i)$ by a simple quadrature. Transforming the entries in terms of the gradients of the shape functions on the reference element yields

$$A_{\mu,T}^{i,j,k,l} = \bar{\mu}_T A_T^{i,j,k,l},$$

where $A_T^{i,j,k,l}$ is the local stiffness matrix for constant viscosities, which is given by

$$\tilde{A}_T^{i,j,k,l} := \frac{1}{6} |\det J_T| \left([J_T^{-1} \hat{\nabla} \hat{\phi}_i]_k \cdot [J_T^{-1} \hat{\nabla} \hat{\phi}_j]_l + \delta_{kl} (J_T^{-1} \hat{\nabla} \hat{\phi}_i) \cdot (J_T^{-1} \hat{\nabla} \hat{\phi}_j) \right),$$

where J_T denotes the Jacobian of the affine element mapping, and $\hat{\nabla} \hat{\phi}_i$ are the gradients of the nodal basis functions with respect to the reference tetrahedron. Now, if our multigrid hierarchy results from a structured refinement of coarse mesh elements by Bey's algorithm [7], the stencils inside the refined elements are composed of element-matrices corresponding to only six distinct types of tetrahedra for each coarse element. These local stiffness matrices can be explicitly stored once per coarse mesh element and the fine-grid stencils can be composed on the fly from these matrices without relying on indirect addressing, since plain array data structures can be employed. Moreover, by a sophisticated averaging procedure, the number of instructions required for the assembly of variable-coefficient stencils can be further reduced. For details, we refer to [29, 26].

A.2. Notes on the assembly of the finite volume operator. As it is common in finite-elements, we consider the element-wise assembly of the stiffness matrix (or stencils in case of matrix-free codes) also for the finite-volume operators. For this, we require only a few standard ingredients that are implemented in any suitable finite-element framework. Consider again a tetrahedron T defined by the vertices \mathbf{x}_i , $i = 0, \dots, 3$. For the ease of presentation, we shall only discuss the construction of the element matrix row associated with the vertex \mathbf{x}_0 , since the other contributions follow by a rearrangement of the local indices.

A.2.1. Facet area normals. We first compute the Jacobian matrix $J_T = [\mathbf{d}_1, \mathbf{d}_2, \mathbf{d}_3]$ with $\mathbf{d}_i := \mathbf{x}_i - \mathbf{x}_0$, and its determinant $\det J_T$. Given the determinant of the element Jacobian $\det J_T$, we immediately know the volume $|T| = \frac{1}{6} |\det J_T|$ of the element and hence the volume of the sub-dual control volumes is given by $B_i^T = \frac{1}{4} |T| = \frac{\sigma}{24} \det J_T$, where $\sigma := \text{sgn}(\det J_T)$ is the sign of the Jacobian determinant. This sign allows us to ensure a consistent orientation of the facet area normals, regardless of the numbering scheme of the code at hand. These facet normals are computed as follows: Consider the control facet γ_{01} which is defined by the element barycenter $\mathbf{p}_0 = \mathbf{x}_T$, the barycenter \mathbf{x}_{01} of the edge between \mathbf{x}_0 and \mathbf{x}_1 , as well as the barycenters of the two element faces attached to this edge $\mathbf{x}_{012} := \frac{1}{3}(\mathbf{x}_0 + \mathbf{x}_1 + \mathbf{x}_2)$ and $\mathbf{x}_{013} := \frac{1}{3}(\mathbf{x}_0 + \mathbf{x}_1 + \mathbf{x}_3)$; cf. Figure 9a for some illustration. This quadrilateral face γ_{01} is planar and hence can be split into the triangles defined by the corner points $\{\mathbf{x}_{01}, \mathbf{x}_{013}, \mathbf{x}_{012}\}$ and $\{\mathbf{x}_T, \mathbf{x}_{012}, \mathbf{x}_{013}\}$. Hence, the unit facet normal \mathbf{n}_{01} scaled with the area of the facet $|\gamma_{01}|$ can be determined as

$$\begin{aligned} \mathbf{n}_{01} |\gamma_{01}| &= \frac{\sigma}{2} ((\mathbf{x}_{013} - \mathbf{x}_{01}) \times (\mathbf{x}_{012} - \mathbf{x}_{01}) + (\mathbf{x}_{012} - \mathbf{x}_T) \times (\mathbf{x}_{013} - \mathbf{x}_T)) \\ &= \frac{\sigma}{2} (\mathbf{x}_T - \mathbf{x}_{01}) \times (\mathbf{x}_{012} - \mathbf{x}_{013}) = \frac{\sigma}{24} (2\mathbf{d}_3 \times \mathbf{d}_2 + \mathbf{d}_1 \times \mathbf{d}_3 + \mathbf{d}_2 \times \mathbf{d}_1), \end{aligned}$$

where we used that $\mathbf{a} \times \mathbf{a} = \mathbf{0}$ and $\mathbf{a} \times \mathbf{b} = -\mathbf{b} \times \mathbf{a}$ as well as the definition of the auxiliary vertices; cf. Figure 9. Proceeding analogously, for the facets γ_{02} and γ_{03} , we obtain

$$\begin{aligned}\mathbf{n}_{01}|\gamma_{01}| &= \frac{\sigma}{24}(2\mathbf{d}_3 \times \mathbf{d}_2 + \mathbf{d}_1 \times \mathbf{d}_3 + \mathbf{d}_2 \times \mathbf{d}_1), \\ \mathbf{n}_{02}|\gamma_{02}| &= \frac{\sigma}{24}(-\mathbf{d}_3 \times \mathbf{d}_2 + 2\mathbf{d}_1 \times \mathbf{d}_3 + \mathbf{d}_2 \times \mathbf{d}_1), \\ \mathbf{n}_{03}|\gamma_{03}| &= \frac{\sigma}{24}(\mathbf{d}_3 \times \mathbf{d}_2 + \mathbf{d}_1 \times \mathbf{d}_3 + 2\mathbf{d}_2 \times \mathbf{d}_1).\end{aligned}$$

Hence, given the entries of the Jacobian, we can easily compute the area facet normals required for the assembly of the entries of the stiffness matrix.

A.2.2. Corrected fluxes. Applying J_T^{-1} , we can evaluate the gradients of the shape functions which are required for the diffusive fluxes as well as for the evaluation of the constant pressure gradient $\nabla p_h|_T$ which is piecewise constant, hence has to be computed once per element. Using this in combination with the facet area normals and an evaluation of the discrete velocity solution at the facet-barycenters, we can perform the integration of (5) by a midpoint quadrature rule for each γ_{0i} , $i = 1, 2, 3$. The evaluation of \mathbf{u}_{0i} at the barycenter of the facet γ_{0i} can be found by barycentric interpolation between the velocity values $\mathbf{u}_i := \mathbf{u}_h(\mathbf{x}_i)$ at the vertices. A straightforward computation yields

$$\begin{aligned}\mathbf{u}_{01} &:= \frac{17}{48}\mathbf{u}_0 + \frac{17}{48}\mathbf{u}_1 + \frac{7}{48}\mathbf{u}_2 + \frac{7}{48}\mathbf{u}_3, \\ \mathbf{u}_{02} &:= \frac{17}{48}\mathbf{u}_0 + \frac{7}{48}\mathbf{u}_1 + \frac{17}{48}\mathbf{u}_2 + \frac{7}{48}\mathbf{u}_3, \\ \mathbf{u}_{03} &:= \frac{17}{48}\mathbf{u}_0 + \frac{7}{48}\mathbf{u}_1 + \frac{7}{48}\mathbf{u}_2 + \frac{17}{48}\mathbf{u}_3.\end{aligned}$$

By combining these ingredients, we find that the net flux across the face γ_{0i} of the control volume can be computed as

$$J_{0i} = (\mathbf{u}_{0i} - \alpha \nabla p_h|_T) \cdot \mathbf{n}_{0i} |\gamma_{0i}|$$

which can then be used to assemble the equation for the global node corresponding to \mathbf{x}_0 . If this is to be done in a matrix-free fashion on structured grids, we can furthermore exploit the grid-structure and symmetries in the nodal patch to save further operations in the cost-intensive parts of the assembly (e.g., factorizing the element Jacobians). Moreover, using a well-known equivalence between finite-element and finite-volume discretizations of diffusion operators [35, Lemma 6.11] we have $\int_T \nabla \phi_i \cdot \nabla \phi_j = -\int_{\partial B_i \cap T} \nabla \phi_i \cdot \mathbf{n}$. Hence, for the assembly of the diffusive fluxes, we can re-use terms that were already computed for the viscous part of the Stokes operator (see Section A.1).

ACKNOWLEDGMENTS

This work was supported by the German Research Foundation (DFG) through the Priority Programme 1648 “Software for Exascale Computing” (SPPEXA). Most numerical examples of Sections 3.1, 3.2, 3.3, and 3.4.1 were obtained using an implementation based on the FEniCS (v. 1.5.0) finite element framework [39].

REFERENCES

- [1] S. BALAY, S. ABHYANKAR, M. F. ADAMS, J. BROWN, P. BRUNE, K. BUSCHELMAN, V. EIJKHOUT, W. D. GROPP, D. KAUSHIK, M. G. KNEPLEY, L. C. MCINNES, K. RUPP, B. F. SMITH, AND H. ZHANG, *PETSc users manual*, Tech. Rep. ANL-95/11 - Revision 3.5, Argonne National Laboratory, 2014.
- [2] J. R. BAUMGARDNER AND P. O. FREDERICKSON, *Icosahedral discretization of the two-sphere*, SIAM Journal on Numerical Analysis, 22 (1985), pp. 1107–1115.
- [3] B. BERGEN, T. GRADL, U. RÜDE, AND F. HÜLSEMANN, *A massively parallel multigrid method for finite elements*, Computing in Science and Engineering, 8 (2006), pp. 56–62.

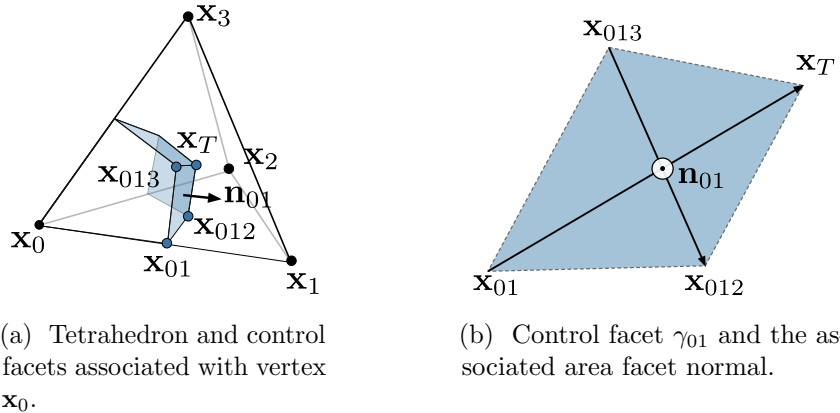


Figure 9. Illustration of the vertices and normals of a control facet.

- [4] B. BERGEN, F. HÜLSEMANN, AND U. RÜDE, *Is 1.7×10^{10} Unknowns the Largest Finite Element System that Can Be Solved Today?*, in ACM/IEEE Proceedings of SC2005: High Performance Networking and Computing, IEEE Computer Society, 2005.
- [5] B. K. BERGEN, T. GRADL, F. HÜLSEMANN, AND U. RÜDE, *A massively parallel multigrid method for finite elements*, Computing in Science and Engineering, 8 (2006), pp. 56–62.
- [6] B. K. BERGEN AND F. HÜLSEMANN, *Hierarchical hybrid grids: data structures and core algorithms for multigrid*, Numerical linear algebra with applications, 11 (2004), pp. 279–291.
- [7] J. BEY, *Tetrahedral grid refinement*, Computing, 55 (1995), pp. 355–378.
- [8] J. BEY, *Finite-Volumen-und Mehrgitterverfahren für elliptische Randwertprobleme*, Springer, 1997.
- [9] J. BEY AND A. REUSKEN, *On the convergence of basic iterative methods for convection–diffusion equations*, Numerical linear algebra with applications, 6 (1999), pp. 329–352.
- [10] B. BLANKENBACH, F. BUSSE, U. CHRISTENSEN, L. CSEREPES, D. GUNKEL, U. HANSEN, H. HARDER, G. JARVIS, M. KOCH, G. MARQUART, ET AL., *A benchmark comparison for mantle convection codes*, Geophysical Journal International, 98 (1989), pp. 23–38.
- [11] P. B. BOCHEV, C. R. DOHRMANN, AND M. D. GUNZBURGER, *Stabilization of low-order mixed finite elements for the Stokes equations*, SIAM Journal on Numerical Analysis, 44 (2006), pp. 82–101.
- [12] D. BOFFI, F. BREZZI, AND M. FORTIN, *Mixed finite element methods and applications*, Springer, 2013.
- [13] F. BREZZI AND J. PITKÄRANTA, *On the stabilization of finite element approximations of the Stokes equations*, in Efficient Solutions of Elliptic Systems, W. Hackbusch, ed., Springer, 1984.
- [14] H. P. BUNGE, M. A. RICHARDS, AND J. R. BAUMGARDNER, *A sensitivity study of three-dimensional spherical mantle convection at 10^8 Rayleigh number: Effects of depth-dependent viscosity, heating mode, and an endothermic phase change*, J. Geophys. Res., 102 (1997), pp. 11991–12007.
- [15] C. BURSTEDDE, G. STADLER, L. ALISIC, L. C. WILCOX, E. TAN, M. GURNIS, AND O. GHATTAS, *Large-scale adaptive mantle convection simulation*, Geophysical Journal International, 192 (2013), pp. 889–906.
- [16] P. G. CIARLET, *The finite element method for elliptic problems*, Elsevier, 1978.
- [17] B. COCKBURN AND C.-W. SHU, *Runge–Kutta discontinuous Galerkin methods for convection-dominated problems*, Journal of Scientific Computing, 16 (2001), pp. 173–261.
- [18] E. M. D’AGNILLO AND L. G. REBOLZ, *On the enforcement of discrete mass conservation in incompressible flow simulations with continuous velocity approximation*, Recent Advances in Scientific Computing and Applications, 586 (2013), p. 143.
- [19] C. DAWSON, S. SUN, AND M. F. WHEELER, *Compatible algorithms for coupled flow and transport*, Computer Methods in Applied Mechanics and Engineering, 193 (2004), pp. 2565–2580.
- [20] D. A. DI PIETRO, S. L. FORTE, AND N. PAROLINI, *Mass preserving finite element implementations of the level set method*, Applied Numerical Mathematics, 56 (2006), pp. 1179–1195.
- [21] H. C. ELMAN, D. J. SILVESTER, AND A. J. WATHEN, *Finite Elements and Fast Iterative Solvers: with Applications in Incompressible Fluid Dynamics*, Oxford University Press, New York, 2005.

- [22] J. FREUND AND R. STENBERG, *On weakly imposed boundary conditions for second order problems*, in Proceedings of the Ninth International Conference on Finite Elements in Fluids, Oct. 1995, pp. 327–336.
- [23] R. W. FREUND, *A transpose-free quasi-minimal residual algorithm for non-Hermitian linear systems*, SIAM Journal on Scientific Computing, 14 (1993), pp. 470–482.
- [24] K. J. GALVIN, A. LINKE, L. G. REBOLZ, AND N. E. WILSON, *Stabilizing poor mass conservation in incompressible flow problems with large irrotational forcing and application to thermal convection*, Computer Methods in Applied Mechanics and Engineering, 237 (2012), pp. 166–176.
- [25] M. GEE, C. SIEFERT, J. HU, R. TUMINARO, AND M. SALA, *ML 5.0 smoothed aggregation user's guide*, Tech. Rep. SAND2006-2649, Sandia National Laboratories, 2006.
- [26] B. GMEINER, *Design and Analysis of Hierarchical Hybrid Multigrid Methods for Peta-Scale Systems and Beyond*, PhD thesis, University of Erlangen-Nuremberg, 2013.
- [27] B. GMEINER, H. KÖSTLER, M. STÜRMER, AND U. RÜDE, *Parallel multigrid on hierarchical hybrid grids: a performance study on current high performance computing clusters*, Concurrency and Computation: Practice and Experience, (doi 10.1002/cpe.2968, 2012).
- [28] B. GMEINER, U. RÜDE, H. STENGEL, C. WALUGA, AND B. WOHLMUTH, *Performance and scalability of hierarchical hybrid multigrid solvers for stokes systems*, SIAM Journal on Scientific Computing, 37 (2015), pp. C143–C168.
- [29] ———, *Towards textbook efficiency for parallel multigrid*, Numerical Mathematics: Theory, Methods and Applications, 8 (2015), pp. 22–46.
- [30] B. GMEINER, C. WALUGA, AND B. WOHLMUTH, *Local mass-corrections for continuous pressure approximations of incompressible flow*, SIAM Journal on Numerical Analysis, 52 (2014), pp. 2931–2956.
- [31] S. GOTTLIEB AND C.-W. SHU, *Total variation diminishing runge-kutta schemes*, Mathematics of Computation of the American Mathematical Society, 67 (1998), pp. 73–85.
- [32] P. P. GRINEVICH AND M. A. OLSHANSKII, *An iterative method for the Stokes-type problem with variable viscosity*, SIAM Journal on Scientific Computing, 31 (2009), pp. 3959–3978.
- [33] S. GROSS, V. REICHELT, AND A. REUSKEN, *A finite element based level set method for two-phase incompressible flows*, Computing and Visualization in Science, 9 (2006), pp. 239–257.
- [34] P. HOUSTON, C. SCHWAB, AND E. SÜLI, *Discontinuous hp-finite element methods for advection-diffusion-reaction problems*, SIAM Journal on Numerical Analysis, 39 (2002), pp. 2133–2163.
- [35] P. KNABNER AND L. ANGERMANN, *Numerical methods for elliptic and parabolic partial differential equations*, Springer, 2003.
- [36] M. KRONBICHLER, T. HEISTER, AND W. BANGERTH, *High Accuracy Mantle Convection Simulation through Modern Numerical Methods*, Geophysics Journal International, 191 (2012), pp. 12–29.
- [37] E. LE MEUR, O. GAGLIARDINI, T. ZWINGER, AND J. RUOKOLAINEN, *Glacier flow modelling: a comparison of the shallow ice approximation and the full-Stokes solution*, Comptes Rendus Physique, 5 (2004), pp. 709–722.
- [38] W. LENG, L. JU, Y. XIE, T. CUI, AND M. GUNZBURGER, *Finite element three-dimensional Stokes ice sheet dynamics model with enhanced local mass conservation*, Journal of Computational Physics, 274 (2014), pp. 299–311.
- [39] A. LOGG, K.-A. MARDAL, AND G. N. WELLS, *DOLFIN: a C++/Python Finite Element Library*, vol. 84 of Lecture Notes in Computational Science and Engineering, Springer, 2012, ch. 10.
- [40] E. OLSSON AND G. KREISS, *A conservative level set method for two phase flow*, Journal of computational physics, 210 (2005), pp. 225–246.
- [41] D. PELLETIER, A. FORTIN, AND R. CAMARERO, *Are FEM solutions of incompressible flows really incompressible? (or how simple flows can cause headaches!)*, Int. J. Numer. Methods Fluids, 9 (1989), pp. 99–112.
- [42] N. PETRA, H. ZHU, G. STADLER, T. J. HUGHES, AND O. GHATTAS, *An inexact Gauss–Newton method for inversion of basal sliding and rheology parameters in a nonlinear Stokes ice sheet model*, Journal of Glaciology, 58 (2012), pp. 889–903.
- [43] Y. RICARD, *Physics of Mantle Convection*, in Treatise of Geophysics, G. Schubert, ed., vol. 7, Elsevier, 2007.
- [44] A. SOULAIMANI AND M. FORTIN, *Finite element solution of compressible viscous flows using conservative variables*, Comput. Methods Appl. Mech. Eng., 118 (1994), pp. 319–350.
- [45] M. SUSSMAN, E. FATEMI, P. SMEREKA, AND S. OSHER, *An improved level set method for incompressible two-phase flows*, Computers & Fluids, 27 (1998), pp. 663–680.

- [46] P. J. TACKLEY, *Dynamics and evolution of the deep mantle resulting from thermal, chemical, phase and melting effects*, Earth-Science Reviews, 110 (2012), pp. 1–25.
- [47] E. TAN, M. GURNIS, L. ARMENDARIZ, L. STRAND, AND S. KIENTZ, *CitcomS User Manual (Version 3.3.0)*, tech. rep., Computational Infrastructure for Geodynamics (CIG), 2014.
- [48] R. VERFÜRTH, *A combined conjugate gradient – multi-grid algorithm for the numerical solution of the Stokes problem*, IMA Journal of Numerical Analysis, 4 (1984), pp. 441–455.
- [49] S. ZHONG, A. McNAMARA, E. TAN, L. MORESI, AND M. GURNIS, *A benchmark study on mantle convection in a 3-D spherical shell using CitcomS*, Geochem. Geophys. Geosyst., 9 (2008), p. Q10017.